



**HAL**  
open science

## Epitaxial graphene morphologies probed by weak (anti)-localization

Ather Mahmood, Cécile Naud, Clément Bouvier, Fanny Hiebel, Pierre Mallet,  
Jean-Yves Veuillen, Laurent Lévy, Didier Chaussende, Thierry Ouisse

► **To cite this version:**

Ather Mahmood, Cécile Naud, Clément Bouvier, Fanny Hiebel, Pierre Mallet, et al.. Epitaxial graphene morphologies probed by weak (anti)-localization. 2012. hal-00705711v1

**HAL Id: hal-00705711**

**<https://hal.science/hal-00705711v1>**

Preprint submitted on 8 Jun 2012 (v1), last revised 1 Mar 2013 (v2)

**HAL** is a multi-disciplinary open access archive for the deposit and dissemination of scientific research documents, whether they are published or not. The documents may come from teaching and research institutions in France or abroad, or from public or private research centers.

L'archive ouverte pluridisciplinaire **HAL**, est destinée au dépôt et à la diffusion de documents scientifiques de niveau recherche, publiés ou non, émanant des établissements d'enseignement et de recherche français ou étrangers, des laboratoires publics ou privés.

# Epitaxial graphene morphologies probed by weak (anti)-localization

A. Mahmood, C. Naud,\* C. Bouvier, F. Hiebel, P. Mallet, J.-Y. Veuillen, and L. P. Lévy†

*Institut Néel, CNRS and Université Joseph Fourier,  
BP 166, 38042 Grenoble Cedex 9, France*

D. Chaussende and T. Ouisse

*Laboratoire des Matériaux et du Génie Physique, CNRS UMR5628 - Grenoble INP,  
Minatec 3 parvis Louis Néel, BP257, 38016 Grenoble, France*

## Abstract

We show how the weak field magneto-conductance can be used as a tool to characterize epitaxial graphene samples grown from the C or the Si face of Silicon Carbide, with mobilities ranging from 120 to 12000 cm<sup>2</sup>/(V.s). Depending on the growth conditions, we observe anti-localization and/or localization which can be understood in term of weak-localization related to quantum interferences. The inferred characteristic diffusion lengths are in agreement with the scanning tunneling microscopy. Finally a graphical representation of the pseudospin diffusion illustrates the observed transition from localization to antilocalization.

---

\*Electronic address: [cecile.naud@grenoble.cnrs.fr](mailto:cecile.naud@grenoble.cnrs.fr)

†Electronic address: [laurent.levy@grenoble.cnrs.fr](mailto:laurent.levy@grenoble.cnrs.fr)

## I. INTRODUCTION

Considerable progress has been achieved in the synthesis of two-dimensional graphene. Since the seminal works [1, 2] which used exfoliated graphite flakes transferred onto  $\text{SiO}_2$  substrates, full wafers of epitaxial graphene can now be grown by high temperature graphitization of Silicon Carbide (SiC) crystals starting either from their Carbon or Silicon face [3]. More recently, MBE growth on SiC substrate [4] and CVD synthesis of large area graphene films have also been achieved on the surface of transition metals in high vacuum [5] or at ambient pressure [6, 7] and their subsequent transfer to a large variety of substrates. These synthesis methods are scalable and offer some real perspectives for micro-electronic applications. A number of characterization techniques are available for the grown layers: STM, AFM, Raman, TEM/SEM and photo-emission have proven their usefulness. On the other hand, the relationship between the growth conditions, the film morphologies and the electronic properties have not yet been systematically investigated [8–16].

In this paper, low field magneto-resistance is used to correlate the transport properties, the growth conditions and the morphologies of epitaxially-grown graphene films elaborated from the different surfaces of 6H-SiC. The films studied have been grown with different graphene layer numbers, both from the Si and C terminated faces, some in ultra-high vacuum other in inert atmospheres. Depending on the SiC polytypes and on the growth conditions, distinct surface morphologies can be observed which lead to very different magnetoresistance behaviors (see figure 1). Exploiting the unique features of interference phenomena present in magneto-transport, electronic properties can be related to the surface morphologies.

## II. LOCALIZATION AND ANTI-LOCALIZATION IN GRAPHENE

Low field magneto-resistance is a sensitive probe for electronic transport as it measures the effect of quantum interferences along closed paths [17]. Depending on the closed loop size, the interferences can be constructive or destructive. For very small loops, it has been demonstrated both theoretically [17, 18] and experimentally [19, 20] that interferences between identical time reversed paths are destructive in graphene leading to a negative magnetoconductance (positive magnetoresistance), which is characteristic of anti-localization of electron waves. For graphene, electron wavefunctions have four components and may

be characterized by two additional quantum numbers: the isospin and the pseudospin. The isospin measures the relative wavefunction amplitude on the equivalent sites (A-B) in graphene unit cell, while the pseudospin measures to which band valley  $K+$  or  $K-$  the quantum states belong [21]. Antilocalization is a characteristic feature of graphene as the isospin (collinear to momentum) undergoes a full rotation on a closed loop, changing the wavefunction sign and so forbidding the backscattering. As the loop size increases, scattering mechanisms lead to additional rotations of the isospin, as well as to the scattering between different valley states, such that the pseudospin need not be preserved on long paths. Two lengthscales characterize this diffusion: the pseudospin is controlled by the intervalley diffusion length  $L_i$ , and  $L_*$  the intravalley diffusion length controls the isospin random diffusion. The “overall” effect of these processes on the interferences along time-reversed paths is to change their sign back to the “normal” positive magneto-conductance due to coherent backscattering [17, 18] observed in other two-dimensional systems. Eventually, for extremely long paths (of length greater than  $L_\varphi$ , the phase coherence length) and/or high temperatures, inelastic scattering kills interferences. The beauty of quantum interference is that a characteristic magnetic field can be associated to every loop size, when half a flux quantum is threaded within the loop area: hence the magnetic fields  $B_{\varphi,i,*} = \frac{\Phi_0}{4\pi L_{\varphi,i,*}^2}$  can be associated to the lengthscales  $L_{\varphi,i,*} = \sqrt{D\tau_{\varphi,i,*}}$  respectively.

It is useful to recall some of the general features of epitaxial graphene on SiC. Graphene layers can be grown by Si sublimation at high temperature [22]. Electrical conduction is known to be dominated by the completed layers closest to the interface [23]. When growing from the SiC C-face, there is a rotation between successive layers which effectively decouples the layers [24, 25]. This is to be contrasted from graphene layers grown from the Si face, where Bernal stacking breaks the symmetry between the two (A-B) carbon sites [22]. In both

TABLE I: Characteristics and extracted parameters of the epitaxial samples studied.

Face	growth	layer #	$\mu(\text{m}^2/(\text{V}\cdot\text{s}))$	$D(\text{m}^2/\text{s})$	$L_\varphi(4\text{K})$	$L_i$	$L_*$
C	UHV	$\leq 5$	0.018	0.0025	72 nm	40 nm	26 nm
C	etched	$\leq 5$	0.018	0.0025	70 nm	40 nm	25 nm
C	Ar	$\approx 50$	1.2	0.159	740 nm		
Si	UHV	2	0.012	0.0022	140 nm	30 nm	18 nm

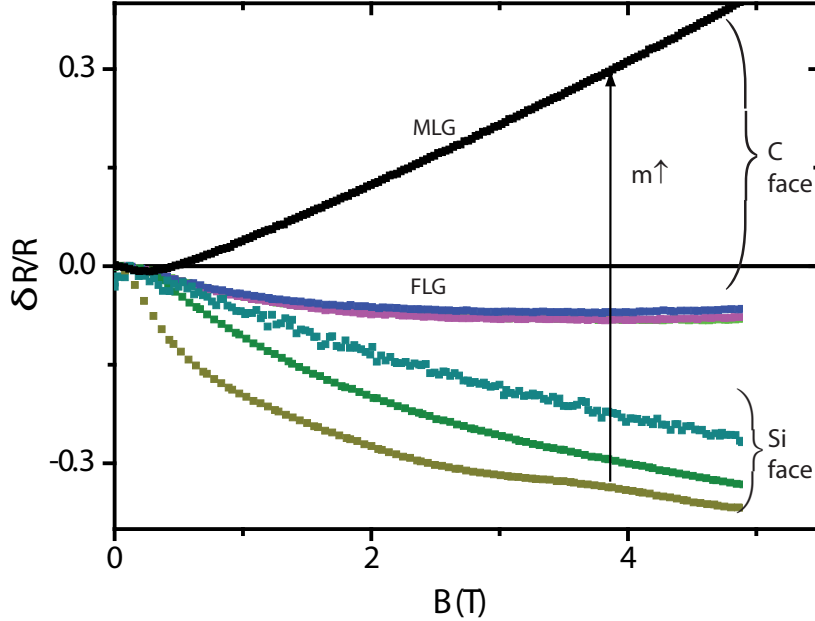


FIG. 1: Overview of the magnetoresistance traces on a large field scale (5T) of 6 graphene epitaxial samples grown in different conditions and measured at 4K. A positive magnetoresistance is observed for the highest mobility ( $m$ ) samples (grown from the SiC C-face), with different slopes for few layers (FLG) (number of layers  $< 10$ ) and multilayer (MLG) (number of layers  $\gg 10$ ) graphene, while negative magnetoresistance are observed on samples grown from the SiC Si-face. All these traces are analyzed quantitatively in this paper and related to the surface morphology.

cases, completed layers are continuous and ripples cover the SiC vicinal steps. Depending on the growth condition, folds are also observed. On ripples or folds, there is a local stretching of the graphene bonds. The other types of known defects arise at the graphene/SiC interface. Defects far from the graphene layer (at distance  $d \gg a$ , where  $a$  is graphene lattice constant) do not break the A-B symmetry and contribute only to intravalley elastic scattering. Sharp potential variations ( $d \approx a$ ), may break the graphene A-B symmetry locally. This scattering potential is time-reversal even and affects simultaneously the isospin and pseudospin and contribute both to the inter and intravalley scattering [17, 18]. Ripples and folds stretch bonds contribute equally to inter and intra valley scattering. Finally, trigonal warping contributes only to intravalley scattering [17, 18].

These scattering processes govern the crossover from localization at low field to anti-localization at high field. The quantum correction [17, 18] to the magneto-conductance

$\delta G = \delta G_i + \delta G_*$  of a single graphene layer can be split between the intervalley

$$\delta G_i = \frac{e^2}{\pi\hbar} \left[ F\left(\frac{B}{B_\varphi}\right) - F\left(\frac{B}{B_\varphi + 2B_i}\right) \right] \quad (1)$$

and the intravalley contributions

$$\delta G_* = -\frac{2e^2}{\pi\hbar} \left[ F\left(\frac{B}{B_\varphi + B_i + B_*}\right) \right], \quad (2)$$

where the function  $F(x) = \ln(x) + \Psi(1/2 + 1/x)$ , and  $\Psi$  is the digamma function.

When the A-B symmetry is fully broken (for a bilayers on Si face, the two sublattices A and B are no more equivalent) the intravalley contributions have the opposite sign  $\delta G = \delta G_i - \delta G_*$ : the magnetoconductance increases monotonously with field and antilocalization disappears [17, 18].

### III. RESULTS AND DISCUSSION

Figure 1 gives an overview of all the magnetoresistance behaviors observed at 4K over a broader range of magnetic field. Films grown from the SiC C-face have larger mobilities and positive magnetoresistance at high fields. Thick films grown from the C-face (top trace) show a linear magnetoresistance at larger fields. The positive magnetoresistance observed at high field for SiC C-face samples can be contrasted with the SiC Si-face graphene which have lower mobilities and a negative magnetoresistance at all fields.

These differences can be understood in terms of weak localization and anti-localization in graphene. Using the appropriate weak-localization formulae, the intervalley, intravalley and phase coherence length can be obtained by fitting the magnetoconductance curves. All the results are summarized in table I and are discussed in the rest of this article.

#### A. Magneto-conductance on the Si-face of 6H-SiC

We first consider samples grown by graphitization of the SiC Si-face. The growth dynamics is slow and the average number of graphene layers can be controlled. When the number of layers exceeds one, the layers stack as in graphite (Bernal) and break the A-B symmetry. In the STM topographical image shown in Figure 2-a, the domains with different number of layers can be precisely identified and labelled. On average, this sample has

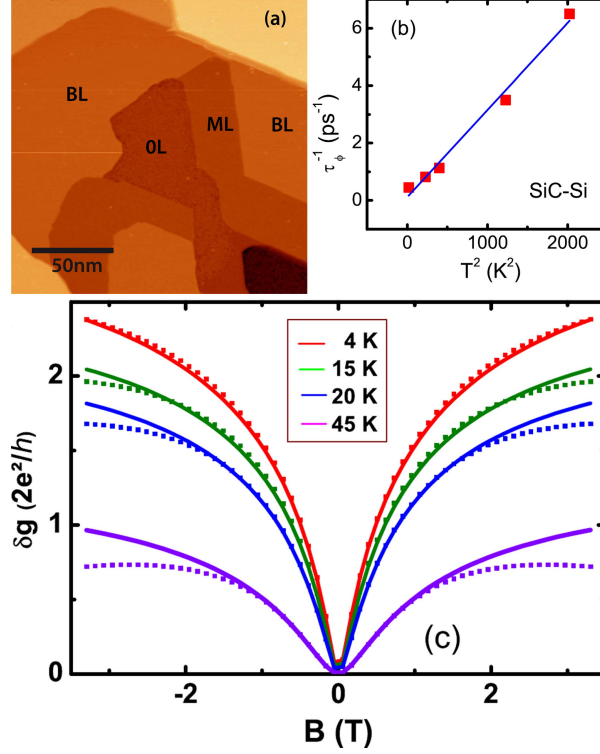


FIG. 2: Graphene sample grown from the SiC Si-face. Top left (a): STM topographic image showing the terraces with different numbers of graphene layers (the labelling as ML for monolayer, BL for bilayer is inferred from the step-height[26]). The average number of layers for this sample is of the order 2 (bilayer). Top right (b): The temperature dependence of the phase coherence length given by the the weak localization fits. The quadratic dependence observed suggests a phonon-dominated dephasing process. Bottom (c): Bilayer magnetoconductance measured at different temperatures (continuous line). The magneto-conductance increases monotonously with field at low  $T$ : it fits the expected quantum correction to the conductance when the A-B symmetry is broken (dashed line).

$\approx 2$  layers and a mobility of 120 cm $^2$ /(V.s). The magnetoconductance traces plotted in units of  $2e^2/h$  for different temperatures are shown in Figure 2-c: the continuous increase observed as a function of field saturates on the scale of  $e^2/h$ . All curves can be fitted with the weak-localization formulae [17, 18]  $\delta G = \delta G_i - \delta G_*$  appropriate for bilayers, assuming that the phase coherence length  $L_\varphi$  is the only temperature dependent parameter. The characteristic field  $B_* = 0.935$  T obtained from the fits is close to twice  $B_i = 0.44$  T. This ratio has been observed in most samples studied. Using  $B_*, B_i$ , the intervalley  $L_i$  and in-

travalley  $L_*$  diffusion lengths are found to be comparable to the size of the flat terraces. This suggests that intervalley and intravalley scattering are dominated by the boundaries between domains. The corresponding timescales  $\tau_{i,*} = L_{\varphi,i,*}^2/(4D)$  are set by the diffusion coefficient  $D$  for this 2D-sample. Using the fits, the dependence of the phase breaking rate  $\tau_{\varphi}^{-1}$  on temperature, is shown in Figure 2-b. The  $T^2$  behavior observed should be contrasted with the linear dependence observed for the C-face [19]. A quadratic increase of  $\tau_{\varphi}^{-1}$  has also been observed at high temperatures by Tikhonenko et al. [20]. The linear contribution due to electron-electron dephasing appears to be quenched by the gap induced by Bernal stacking, leaving another scattering mechanism, probably associated with phonons, as the dominant one. For semiconductor 2D electronic systems, the electron-phonon scattering rate is known both from theory and experiments to increase as  $T^3$ . For isolated graphene planes, different regimes [27] have been identified depending on the relative value of the temperature compared to the Bloch-Grüneisen temperature  $T_{BG} = 2k_F v_{ph}/k_B$  ( $\approx 90K$  for this sample): below  $T_{BG}$ , the rate grows as  $T^4$ , while it is linear above [28]. How the SiC substrate affects this behavior is not known. While the fits (Figure 2-c) are quite accurate at low fields, deviations can be observed at high temperature and high fields: a negative component in the magnetoresistance traces grows at large fields as the temperature is raised. The origin of this classical-like behavior is not clear, but it is concomitant with the appearance of the quadratic dephasing rate.

## B. Magneto-conductance on the C-face of 6H-SiC

Samples grown from SiC C-face have notably different morphologies when grown in high vacuum or in an inert atmosphere. When grown in ultra-high vacuum, flat terraces are relatively small as shown on the topographic STM image (Figure 3-d top-left), typically of order 60 nm with folds and ripples at their boundaries. When grown in an inert atmosphere, the domains (and mobilities) are much larger (see figure 4).

As long as the number of layers is small ( $\leq 10$ ), it is possible to analyze the magneto-conductance in term of the weak localization-antilocalization effects discussed above, in agreement with earlier studies [15, 19, 20]. This is illustrated in the bottom panel of Figure 3-f, where the magnetoconductance traces of a UHV grown sample, scaled in units of  $2e^2/h$ , are plotted for different temperatures. All traces can be fitted to the weak localization correction



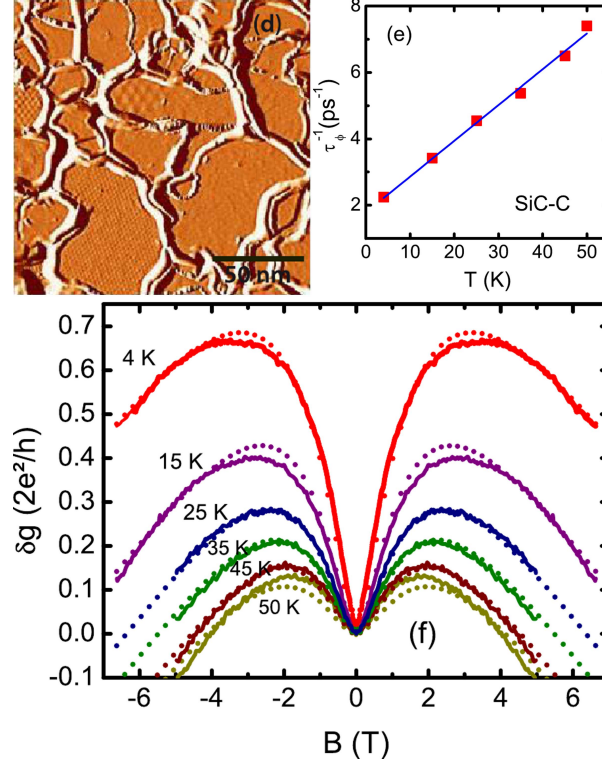


FIG. 3: Graphene sample grown from SiC C-face. Top left (d) : Derivative STM image (200 nm $\times$ 200 nm) showing the surface morphology of a sample graphitized in UHV. The flat terraces are of the order of 60 nm in size and are separated by ripples and folds. Top right (e): temperature dependence of the dephasing rate on the carbon face. Bottom (f): The magnetoconductance traces of C-face grown samples show a weak localization dip (probing the longest coherent loops) close to zero field and a negative magnetoconductance at higher field (anti-localization for short loops). The crossover regime occurs around the field  $B_* \approx 2B_i$ . At higher temperature, long loops are cut-off ( $L_\phi$  decreases at higher  $T$ ) reducing the weak localization contribution at low field. The contrast with the Si face (Fig. 2-c) is quite clear.

discussed in equations 1 and 2. In particular, the weak localization dip observed at low field (i.e. for the longest coherent retrodiffusion loops) turns into a negative magnetoconductance at higher fields (anti-localization for small retrodiffusion loops). The characteristic field  $B_* \approx 1.8$  T is found to be nearly twice  $B_i \approx 0.72$  T as for the Si-face grown samples. The corresponding intervalley  $L_i$  and intravalley  $L_*$  diffusion length are also of the order of the size of the flat terraces (see the table I). All traces can be fitted assuming that only  $L_\phi$  varies with temperature. The dependence of the dephasing rate  $\tau_\phi^{-1}$  with  $T$  is shown in Figure

3-e. The linear temperature dependence, also observed in Wu et al. [19] is consistent with Altshuler-Aronov prediction for electron-electron interactions [29, 30]  $\frac{h}{\tau_\varphi} = \frac{k_B T}{2\pi} \frac{R_\square}{R_K} \ln\left(\frac{\pi R_K}{R_\square}\right)$  with  $R_K = h/e^2$  is the quantum resistance and  $R_\square$  is the square resistance. The measured slope ( $\approx 8 \times 10^{10} \text{s}^{-1} \text{K}^{-1}$ ) is an order of magnitude larger than the expected value. Similar discrepancies are not uncommon in other semiconducting 2DEG systems. Among the other sources of dephasing, the Coulomb scattering of electrons in different layers have been shown theoretically to be relevant [31]. Electron-phonon scattering may also contribute [27, 28].

### C. Quantum wires

The 2D graphene films were etched in wires of width  $w \approx 1 - 2 \mu\text{m}$  with Hall probe geometries and the temperature dependence of the magnetoconductance were measured using four probes. The values of  $L_i$ ,  $L_*$  and  $L_\varphi$  extracted from the weak localization analysis using the 2D formulae are remarkably close to the values obtained for un-etched films (see table I). This is expected [18], since the crossover to a 1D behavior becomes perceptible for wires narrower than  $L_\varphi$ , when the characteristic field  $B_\varphi$  becomes  $B_\varphi \rightarrow \frac{\Phi_0}{4\pi w L_\varphi}$ . Since the phase coherence length of our films is less than 100 nanometers, the crossover occurs for very narrow wires. For larger width, the only effect of etching is in the additional scattering induced by processing (wire edges, residues), which appears here to be small.

### D. Thick graphene sample

We now turn to samples graphitized from the SiC C-face in an inert atmosphere which have significantly different morphologies and transport behaviors. When graphitizing from the SiC C-face, the number of layers increases rapidly and a larger number of graphene layers (of order of 30-50 for the sample studied) is reached in a 10 minutes period. After annealing at high temperature, the sample morphology (as shown in the AFM image 4-inset) shows very large (several  $\mu\text{m}$ ) domains separated by fold or ripples. The magnetoconductance traces measured at different temperatures are shown in Figure 4. A narrow weak localization dip close to zero field is clearly seen: its width is controlled by the phase coherence length  $L_\varphi$  (of the order of 750 nm at 4 K). The diffusion coefficient ( $1600 \text{ cm}^2/\text{s}$ ) and mobilities ( $10^4 \text{ cm}^2/(\text{V}\cdot\text{s})$ ) are also found to be much larger than in the UHV grown samples.

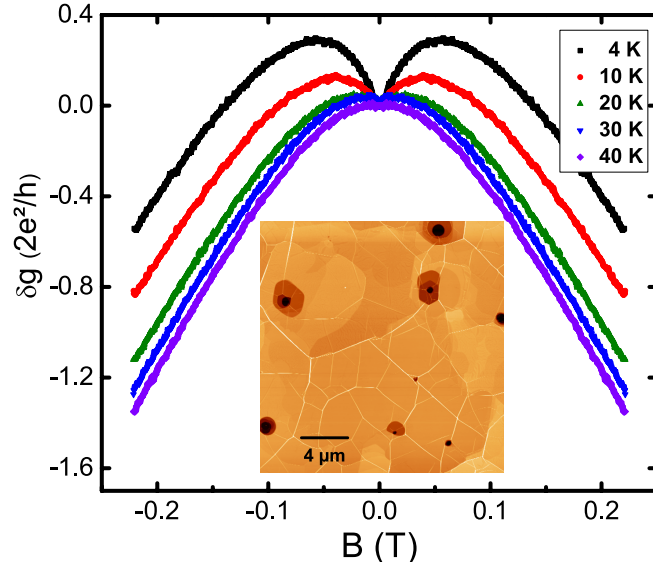


FIG. 4: Magneto-conductance of a thick graphene stack, annealed at high temperature. A narrow weak localization dip close to zero field is observed at low temperature. Above 0.05 T, the negative magnetoconductance cannot be attributed to weak-localization alone. The data is consistent with classical reduction of the longitudinal conductance for electron with relativistic dynamics (see text). Inset: AFM image of the sample showing large (several microns) domains separated by ripples. The holes (black dots) are about 30-40 nm deep.

Within this thick sample, the conduction is no longer limited to the layer closest to the interface with the SiC. From the measured value of the diffusion coefficient, we infer a large mean free path  $\ell_e \approx 300\text{nm}$  which is comparable to  $L_\phi$ . A fit to the magnetoconductance shown in Fig. 4 gives a scattering time  $\tau_L \approx 0.05\text{ps}$  shorter than the mean-free time  $\tau_e \approx 0.3\text{ps}$  suggesting other scattering processes are at play in a magnetic field (Coulomb scattering between layers [31], tunneling between graphene plane) which contribute to the broadening of Landau levels and shorten the effective scattering times. The amplitude of the negative magnetoconductance above 0.05 T shown in Fig. 4 also exceeds  $e^2/h$  and cannot be attributed to quantum interference alone. Assuming relativistic electron dynamics, the cyclotron radius  $r_c = v_F/\omega_c = \ell_B/\sqrt{2}$  becomes smaller than the mean free path for fields exceeding ( $B_c \approx 10^{-1}$  T). As seen in Fig. 4, the magnetoconductance turns negative above 0.05 T ( $> B_c$ ). At larger field ( $> 0.4T$ ), a linear magnetoresistance regime is observed (the top curve in Fig. 1), which is consistent with previous transport measurements on epitaxial graphene [32]. Several routes to linear magnetoconductance have been previously consid-

ered. For inhomogeneous and disordered materials, a classical resistor network model [33, 34] accounts for the linear magnetoresistance observed in silver chalcogenides. Another mechanism leading to a linear magnetoconductance has been considered by Abrikosov[35, 36] for layered materials and small (and zero) gap 3d-semiconductors: in the quantum limit, when the temperature and Fermi energy are smaller than the Landau band splitting, the magnetoresistance becomes linear. For a pure 2d system, the requirements for quantum linear magnetoresistance coincide with the quantum Hall regime. On these samples, the onset of the linear regime (0.5 T) which coincides approximatively to  $\omega_c\tau_L \geq 1$  occurs well before the Shubnikov-de Haas oscillations are observed. This indicates that tunneling between layers is larger in these thick graphene samples compared to the few layer samples (number of layers  $< 10$ ). This makes the Abrikosov mechanism the most probable explanation for the linear magnetoresistance, in agreement with Ref.[32].

From a device point of view, the transport characteristics of such thick graphene stack are good. Gating effects measured on such thick graphene stacks have however been found to be small.

### E. General remarks

The quasiparticles of graphene can be described in the space of four-component wave functions,  $|A\rangle_{K+}, |B\rangle_{K+}, |B\rangle_{K-}, |A\rangle_{K-}$  basis describing electronic amplitude on  $A$  and  $B$  sites and in the valleys  $K+$  and  $K-$ . In order to describe the microscopic scattering potentials, we introduce two sets of  $4 \times 4$  hermitian matrices : the isospin ( $\vec{\Sigma} = (\Sigma_x, \Sigma_y, \Sigma_z)$ ) and the pseudospin ( $\vec{\Lambda} = (\Lambda_x, \Lambda_y, \Lambda_z)$ ) [17, 18]. Then the electron hamiltonian in weakly disorder graphene can be parameterized as

$$V(\vec{r}) = u_0(\vec{r})\hat{\mathbf{I}} + \sum_{i,j} u_{i,j}(\vec{r})\Lambda_i\Sigma_j (i, j \equiv x, y, z) \quad (3)$$

For each scattering potential  $u_{i,j}(\vec{r})$ , there is a microscopic scattering rate  $\tau_{ij}^{-1}$ . Since  $x$  and  $y$  are equivalent ( $\perp$ ), there are only four microscopic scattering rates,  $\tau_{zz}^{-1}, \tau_{z\perp}^{-1}, \tau_{\perp z}^{-1}$  and  $\tau_{\perp\perp}^{-1}$ . If the sample is sufficiently disordered, it is plausible to assume that all the potential  $u_{ij}$  and scattering rates  $\tau_{ij}^{-1}$  are comparable. In this limit, the inter and intravalley scattering rates [18]  $\tau_i^{-1} = 4\tau_{\perp\perp}^{-1} + 2\tau_{z\perp}^{-1} \approx 6\tau_0^{-1}$  and  $\tau_*^{-1} = \tau_i^{-1} + 2\tau_z^{-1} \approx 12\tau_0^{-1}$  since  $\tau_z = 2\tau_{zz}^{-1} + \tau_{\perp z}^{-1}$ .

$B_* = \frac{\Phi_0}{4\pi D\tau_*}$  is found to be twice  $B_i = \frac{\Phi_0}{4\pi D\tau_i}$  in agreement with our experimental results, and the weak localization correction depends only on  $B_*$  as  $B_\varphi \xrightarrow{T \rightarrow 0} 0$ : there is a universal scaling of the magnetoconductance in  $B/B_*$  and all samples-magnetoconductances collapse on this curve at low temperatures.

#### IV. BLOCH SPHERE REPRESENTATION

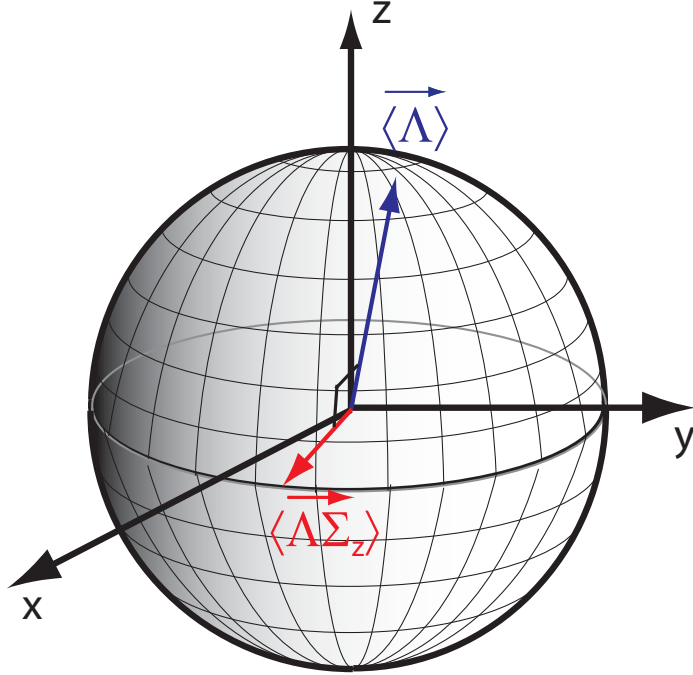


FIG. 5: “Bloch representation” of the pseudospin rotations for a closed loop. The initial electron state is in the  $K$ -isospin valley ( $\hat{z}$ ). After forward propagation along the loop, the pseudospin  $\langle \vec{\Lambda} \rangle$  rotates and its magnitude is less than unity. The vector  $\langle \vec{\Lambda} \Sigma_z \rangle$  is perpendicular to  $\langle \vec{\Lambda} \rangle$ . Their norms are such that  $|\langle \vec{\Lambda} \rangle|^2 + |\langle \vec{\Lambda} \Sigma_z \rangle|^2 = 1$  for forward and backward propagation. The pseudospins are not collinear for the two time-reversed propagation path and this affects their interferences.

For massive electrons, the effect of diffusion on the electron spins can be represented as a random walk on the Bloch sphere [37, 38]. In this semiclassical picture, the spin-diffusion length is reached when the spin has diffused over the entire Bloch sphere. For graphene, there are two internal degrees of freedom, pseudospin ( $\vec{\Lambda}$ ) and isospin ( $\vec{\Sigma}$ ), which are affected by intravalley and intervalley scattering when diffusing over time-reversed loops. A Bloch representation of their diffusive motion can still be used using two vectors,  $\langle \vec{\Lambda} \rangle$ ,

the expectation value of the pseudospin and a second vector  $\langle \vec{\Lambda} \Sigma_z \rangle$ .

For sake of simplicity, we assume that, in Eq.3, the scattering potentials  $u_{z\perp}$  and  $u_{\perp\perp}$  equal and approximately equal to zero. The remaining terms  $u_{zz}$  account for the local A-B symmetry breaking while  $u_{\perp z}$  describes a local graphene bond stretching. The local scattering potential becomes

$$V(\vec{r}) = u_0(\vec{r})\hat{\mathbf{I}} + u(\vec{r})\hat{n} \cdot \vec{\Lambda} \Sigma_z. \quad (4)$$

The dominant first term accounts for potential diffusion while the second term specifies the relative magnitude of bond stretching potential to the symmetry breaking potential leading to intra and intervalley scattering.

As shown explicitly in the appendix, the pseudospin  $\langle \vec{\Lambda} \rangle$  and  $\langle \vec{\Lambda} \Sigma_z \rangle$  rotate at each collision, but stay always orthogonal to each other for this generic scattering potential. Furthermore, their norm is preserved to unity

$$\langle \vec{\Lambda} \rangle \cdot \langle \vec{\Lambda} \Sigma_z \rangle = 0, \quad (5)$$

$$|\langle \vec{\Lambda} \rangle|^2 + |\langle \vec{\Lambda} \Sigma_z \rangle|^2 = 1 \quad (6)$$

so the two vectors are always inside the Bloch sphere.

For valley eigenstates,  $\langle \vec{\Lambda} \rangle = (0, 0, \pm 1)$  and  $\langle \vec{\Lambda} \Sigma_z \rangle = 0$ . After a diffusion sequence along a closed path, this vector rotates off the  $\hat{z}$  axis (see Figure 5), and  $\langle \vec{\Lambda} \Sigma_z \rangle$  become non-zero and orthogonal to  $\langle \vec{\Lambda} \rangle$ .

When diffusing on the time reversed path, the order of successive pseudo-spin rotation is not the same, and  ${}_T\langle \vec{\Lambda} \rangle_T$ ,  ${}_T\langle \vec{\Lambda} \Sigma_z \rangle_T$  are not collinear with the forward propagation image  $\langle \vec{\Lambda} \rangle$  and  $\langle \vec{\Lambda} \Sigma_z \rangle$  respectively. If the pseudo-spin rotation remains small (short loops), these vectors remains close to valley eigenstates ( $\hat{z}$ ) and the interference (antilocalization) is not affected. On the other hand, for longer loops, intravalley and intervalley scattering both contribute in the interference term, leading to the change of sign predicted by diagrammatic theory and discussed in the experiment.

## V. CONCLUSIONS

In this paper, an overview of weak localization properties on a variety of epitaxially grown samples has been presented. For all types of few-layers graphene samples, the measured

characteristic lengthscales for iso and pseudo-spin diffusion (intra/intervalley scattering) coincide with the terrace and or domain sizes identified on the samples STM or AFM images. For most samples, the magnitude of the intervalley and intravalley scattering rates have a ratio of 2. Such a ratio is found when all scattering rates  $\tau_{ij}^{-1}$  induced by the scattering potentials (cf. Eq. 3)  $\tau_{ij}^{-1}$  ( $i, j \equiv, z, \perp$ ) are of similar magnitude. This suggests that most of the diffusion occurs at the edges of the terraces where all types of scattering processes are present.

A graphic representation of the pseudospin diffusion on a Bloch sphere can be constructed in analogy with the one used for spin-diffusion in ordinary metals. This picture is fully consistent with the diagrammatic analysis [17, 18].

### Appendix: Pseudospin diffusion

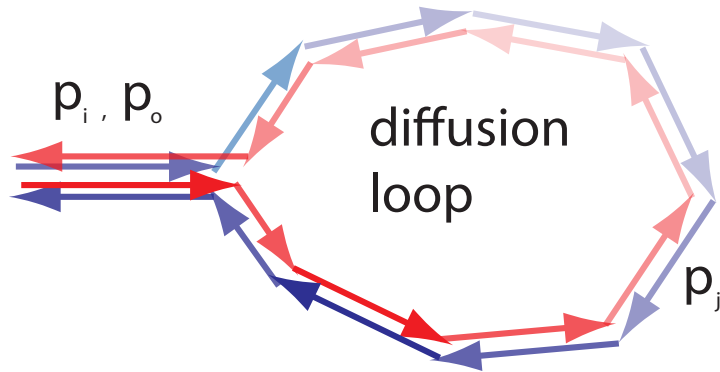


FIG. 6: Sequence of momentum scattering events on defects, showing explicitly the interfering time-reversed paths which add coherently and contribute to weak (anti)localization. The size of the contributing loops are cut off by the coherence length,  $L_\phi = \sqrt{D\tau_\phi}$

The opposite momenta eigenstates in each pseudospin valley are also isospin eigenstates which is collinear with the momentum direction. If  $\vec{p}$  makes an angle  $\phi$  with respect to the axis  $\hat{x}$  the momenta eigenstates in each valley are

$$\begin{aligned} |\vec{p}\rangle_{K\pm} &= e^{(i\vec{p}\cdot\vec{r}/\hbar)} e^{(-i\frac{\phi}{2}\Sigma_z)} |\hat{x}\rangle_{K\pm} \\ |-\vec{p}\rangle_{K\pm} &= e^{(-i\vec{p}\cdot\vec{r}/\hbar)} e^{(-i\frac{\phi}{2}\Sigma_z)} |-\hat{x}\rangle_{K\pm} \end{aligned} \quad (\text{A.1})$$

where  $|\hat{x}\rangle_{K\pm} = \frac{1}{\sqrt{2}}(\pm 1, 1)$  are the isospin eigenstates pointing the  $\hat{x}$  direction. Explicitly, in the isospin/pseudospin space ( $|A\rangle_{K+}, |B\rangle_{K+}, |B\rangle_{K-}, |A\rangle_{K-}$ ) the momenta eigen-

states can be written for the  $K_+$  valley,  $|\vec{p}\rangle_{K_+} = e^{(i\frac{\vec{p}\cdot\vec{r}}{\hbar})} \left( e^{-i\frac{\phi}{2}}, e^{i\frac{\phi}{2}}, 0, 0 \right)$ ,  $|- \vec{p}\rangle_{K_+} = e^{(-i\frac{\vec{p}\cdot\vec{r}}{\hbar})} \left( -e^{-i\frac{\phi}{2}}, e^{i\frac{\phi}{2}}, 0, 0 \right)$  and for  $K_-$  the valley,  $|\vec{p}\rangle_{K_-} = e^{(i\frac{\vec{p}\cdot\vec{r}}{\hbar})} \left( 0, 0, e^{i\frac{\phi}{2}}, -e^{-i\frac{\phi}{2}} \right)$ ,  $|- \vec{p}\rangle_{K_-} = e^{(-i\frac{\vec{p}\cdot\vec{r}}{\hbar})} \left( 0, 0, e^{-i\frac{\phi}{2}}, e^{i\frac{\phi}{2}} \right)$ .

The isospin  $\vec{\Sigma}$  and pseudospin  $\vec{\Lambda}$  operators commute with each-other and are generators for rotation in the isospin and pseudospin spaces. Their matrix representations in isospin/pseudospin space are

$$\Lambda_x = \begin{pmatrix} 0 & 0 & 1 & 0 \\ 0 & 0 & 0 & -1 \\ 1 & 0 & 0 & 0 \\ 0 & -1 & 0 & 0 \end{pmatrix}, \Lambda_y = \begin{pmatrix} 0 & 0 & -i & 0 \\ 0 & 0 & 0 & i \\ 1 & 0 & 0 & 0 \\ 0 & -i & 0 & 0 \end{pmatrix} \quad (\text{A.2})$$

$$\Lambda_z = \begin{pmatrix} 1 & 0 & 0 & 0 \\ 0 & 1 & 0 & 0 \\ 0 & 0 & -1 & 0 \\ 0 & 0 & 0 & -1 \end{pmatrix}, \Sigma_z = \begin{pmatrix} 1 & 0 & 0 & 0 \\ 0 & -1 & 0 & 0 \\ 0 & 0 & 1 & 0 \\ 0 & 0 & 0 & -1 \end{pmatrix} \quad (\text{A.3})$$

A weak localization-loop in momentum space, shown in 6, is a sequence of momenta ending with momentum  $\vec{p}_o$  in the opposite direction as the initial momentum  $\vec{p}_i$ . For each scattering  $\vec{p} \rightarrow \vec{p}'$  event, the scattering amplitudes on the iso/pseudospin can be represented by

$$F_{\vec{p}',\vec{p}}^{op} \approx f_{\vec{p}',\vec{p}} \left( \mathbf{1} + i\frac{\chi}{2} \hat{n}_j \cdot \vec{\Lambda} \Sigma_z \right) \quad (\text{A.4})$$

where we have assumed that the scalar term in 4 dominates the scattering amplitude ( $\chi \ll 1$ ).  $\hat{n}_j$  is a local axis describing the nature (intra/intervalley) of the pseudospin diffusion occurring at site  $j$ .

The operators  $\vec{\Lambda}$  and  $\vec{\Lambda} \Sigma_z$  form a Lie algebra  $[\Lambda_\alpha \Sigma_z, \Lambda_\beta \Sigma_z] = i\epsilon^{\alpha\beta\gamma} \Lambda_\gamma$   $[\Lambda_\alpha, \Lambda_\beta \Sigma_z] = i\epsilon^{\alpha\beta\gamma} \Lambda_\gamma \Sigma_z$ , and can be used to represent the effect of rotations in the isospin/pseudospin space.

At each collision  $j$ , the elementary rotation can be represented by the unitary operator ( $\vec{\Lambda}$  and  $\Sigma_z$  commute)

$$D(\chi_j, \hat{n}_j) = e^{i\frac{\chi_j}{2} \hat{n}_j \cdot \vec{\Lambda} \Sigma_z} = \cos \frac{\chi_j}{2} + i \hat{n}_j \cdot \vec{\Lambda} \Sigma_z \sin \frac{\chi_j}{2}. \quad (\text{A.5})$$

Starting from the eigenstate  $|p\rangle_{K_+}$  for which  $\langle \vec{\Lambda} \rangle = \hat{z}$  and  $\langle \vec{\Lambda} \Sigma_z \rangle = 0$ , this state becomes  $D(\chi, \hat{n})|p\rangle_{K_+}$  after a collision. After completing a weak localization loop, the cumulative



effect on the iso/pseudospin is a product matrix of the sequence of  $D(\chi_j, \hat{n}_j)$ , which can be decomposed in elementary ones, because  $\vec{\Lambda}$  and  $\vec{\Lambda}\Sigma_z$  form a Lie algebra. This leads to rotations of the expectation value of  $\langle\vec{\Lambda}\rangle$  and  $\langle\vec{\Lambda}\Sigma_z\rangle$ . These vectors can be used to represent graphically the effect of collision in iso/pseudospin space. For any series of collisions, they are orthogonal vectors  $\langle\vec{\Lambda}\rangle \cdot \langle\vec{\Lambda}\Sigma_z\rangle = 0$  and the norm  $|\langle\vec{\Lambda}\rangle|^2 + |\langle\vec{\Lambda}\Sigma_z\rangle|^2 = 1$  is preserved. The effect of scattering on iso/pseudospin variables can therefore be tracked by plotting the expectation values of  $\vec{\Lambda}$ ,  $\vec{\Lambda}\Sigma_z$  and  $\vec{\Sigma}$  after each collision.

When propagating over the time-reversed path, isospin and pseudospins do not rotate in the same direction because the  $\vec{\Lambda}$  and  $\vec{\Lambda}\Sigma_z$  do not commute:  ${}_T\langle\vec{\Lambda}\rangle_T, {}_T\langle\vec{\Lambda}\Sigma_z\rangle_T$  are not collinear with the forward propagation image. An arbitrary rotation in real space is the product of three elementary rotation: a rotation by an angle  $\alpha$  around the  $\hat{z}$  axis (representing an intravalley diffusion), a rotation by an angle  $\chi$  around the line of node  $\hat{x}'$ , (representing a pure intervalley diffusion) and a final rotation by an angle  $\beta$  around  $\hat{z}'$ . Using the parametrization of the iso-pseudospin diffusion in term of the isospin rotation angles  $\alpha, \beta$  and the pseudospin rotation angle  $\chi$ , the interference term between the amplitudes of two time-reversed closed paths threaded by a magnetic flux  $\Phi$  is

$$2 \cos 2\varphi(1 - \cos \chi) - 4 \cos(\alpha + \beta + \chi + 2\varphi), \quad (\text{A.6})$$

where  $\varphi = 2\pi\frac{\Phi}{\Phi_0}$  is the loop Aharonov-Bohm phase. The first term in A.6 depends only on the pseudospin rotation angle (intervalley) and leads to the intervalley (Eq. 1) contribution to weak-localization. The second term depends on intravalley and intervalley in the same way as Eq. 2. For small loops, all angles  $\alpha, \beta$  and  $\chi$  are small: the last term dominates yielding weak-antilocalization. In the other limit, this last term averages to zero and normal localization is recovered.

## Acknowledgments

This work is supported by the French National Research Agency (GraphSiC and XP-graphene projects) and the Nanosciences Foundation (DISPOGRAPH project).

---

- [1] K. S. Novoselov, A. K. Geim, S. V. Morozov, D. Jiang, M. I. Katsnelson, I. V. Grigorieva, S. V. Dubonos, and A. A. Firsov, *Nature* **438**, 197 (2005).
- [2] Y. B. Zhang, Y. W. Tan, H. L. Stormer, and P. Kim, *Nature* **438**, 201 (2005).
- [3] C. Berger, Z. M. Song, T. B. Li, X. B. Li, A. Y. Ogbazghi, R. Feng, Z. T. Dai, A. N. Marchenkov, E. H. Conrad, P. N. First, and W. A. de Heer, *Journal of Physical Chemistry B* **108**, 19912 (2004).
- [4] E. Moreau, F. J. Ferrer, D. Vignaud, S. Godey, and X. Wallart, *Physica Status Solidi a-Applications and Materials Science* **207**, 300 (2010).
- [5] J. Coraux, A. T. N'Diaye, C. Busse, and T. Michely, *Nano Letters* **8**, 565 (2008).
- [6] K. S. Kim, Y. Zhao, H. Jang, S. Y. Lee, J. M. Kim, K. S. Kim, J. H. Ahn, P. Kim, J. Y. Choi, and B. H. Hong, *Nature* **457**, 706 (2009).
- [7] X. S. Li, W. W. Cai, J. H. An, S. Kim, J. Nah, D. X. Yang, R. Piner, A. Velamakanni, I. Jung, E. Tutuc, S. K. Banerjee, L. Colombo, and R. S. Ruoff, *Science* **324**, 1312 (2009).
- [8] J. A. Robinson, M. Wetherington, J. L. Tedesco, P. M. Campbell, X. Weng, J. Stitt, M. A. Fanton, E. Frantz, D. Snyder, B. L. VanMil, G. G. Jernigan, R. L. Myers-Ward, C. R. Eddy, and D. K. Gaskill, *Nano Letters* **9**, 2873 (2009).
- [9] T. Low, V. Perebeinos, J. Tersoff, and P. Avouris, *Phys. Rev. Lett.* **108**, 096601 (2012).
- [10] S. Tanabe, Y. Sekine, H. Kageshima, M. Nagase, and H. Hibino, *Applied Physics Express* **3**, 1 (2010).
- [11] S.-H. Ji, J. B. Hannon, R. M. Tromp, V. Perebeinos, J. Tersoff, and F. M. Ross, *Nature Materials* **11**, 114 (2012).
- [12] Y.-M. Lin, C. Dimitrakopoulos, D. B. Farmer, S.-J. Han, Y. Wu, W. Zhu, D. D. Kurt Gaskill, J. L. Tedesco, M.-W. R. L., C. R. Eddy, A. Gril, and P. Avouris, *Applied Physics Letters* **97**, 112107 (2010).
- [13] K. Lee, S. Kim, M. S. Points, T. E. Beechem, T. Oht, and E. Tutuc, *NanoLetters* **11**, 3624

- (2011).
- [14] J. Jobst, D. Waldmann, F. Speck, R. Hirner, D. K. Maude, T. Seyller, and H. B. Weber, *Phys. Rev. B* **81**, 195434 (2010).
  - [15] G. L. Creeth, A. J. Strudwick, J. T. Sadowski, and C. H. Marrows, *Phys. Rev. B* **83**, 195440 (2011).
  - [16] S. Lara-Avila, A. Tzalenchuk, S. Kubatkin, R. Yakimova, T. J. B. M. Janssen, K. Cedergren, T. Bergsten, and V. Fal'ko, *Phys. Rev. Lett.* **107**, 166602 (2011).
  - [17] E. McCann, K. Kechedzhi, V. I. Fal'ko, H. Suzuura, T. Ando, and B. L. Altshuler, *Physical Review Letters* **97**, 146805 (2006).
  - [18] K. Kechedzhi, E. McCann, V. I. Fal'ko, H. Suzuura, T. Ando, and B. L. Altshuler, *European Physical Journal-Special Topics* **148**, 39 (2007).
  - [19] X. S. Wu, X. B. Li, Z. M. Song, C. Berger, and W. A. de Heer, *Physical Review Letters* **98**, 136801 (2007).
  - [20] F. V. Tikhonenko, A. A. Kozikov, A. K. Savchenko, and R. V. Gorbachev, *Physical Review Letters* **103**, 226801 (2009).
  - [21] A. H. Castro Neto, F. Guinea, N. M. R. Peres, K. S. Novoselov, and A. K. Geim, *Reviews of Modern Physics* **81**, 109 (2009).
  - [22] J. Hass, W. A. de Heer, and E. H. Conrad, *Journal of Physics-Condensed Matter* **20**, 323202 (2008).
  - [23] C. Berger, Z. M. Song, X. B. Li, X. S. Wu, N. Brown, C. Naud, D. Mayou, T. B. Li, J. Hass, A. N. Marchenkov, E. H. Conrad, P. N. First, and W. A. de Heer, *Science* **312**, 1191 (2006).
  - [24] J. Hass, F. Varchon, J. E. Millan-Otoya, M. Sprinkle, N. Sharma, W. A. De Heer, C. Berger, P. N. First, L. Magaud, and E. H. Conrad, *Physical Review Letters* **100**, 125504 (2008).
  - [25] C. Faugeras, A. Nerriere, M. Potemski, A. Mahmood, E. Dujardin, C. Berger, and W. A. de Heer, *Applied Physics Letters* **92**, 0119214 (2008).
  - [26] P. Lauffer, K. V. Emtsev, R. Graupner, T. Seyller, L. Ley, S. A. Reshanov, and H. B. Weber, *Physical Review B* **77**, 155426 (2008).
  - [27] E. H. Hwang and S. Das Sarma, *Physical Review B* **77**, 115449 (2008).
  - [28] T. Stauber, N. M. R. Peres, and F. Guinea, *Physical Review B* **76**, 205423 (2007).
  - [29] B. L. Altshuler and A. Aronov, in *Electron-Electron Interactions in Disordered Systems*, Modern problems in condensed matter science, Vol. 10, edited by A. L. P. M. Efros (North-Holland,

Amsterdam, 1985) pp. 1–150.

- [30] I. L. Aleiner, B. L. Altshuler, and M. E. Gershenson, *Waves in Random Media* **9**, 201 (1999).
- [31] P. Darancet, N. Wipf, C. Berger, W. A. de Heer, and D. Mayou, *Physical Review Letters* **101**, 116806 (2008).
- [32] A. L. Friedman, J. L. Tedesco, P. M. Campbell, J. C. Culbertson, E. Aifer, F. K. Perkins, R. L. Myers-Ward, J. K. Hite, C. R. Eddy, G. G. Jernigan, and D. K. Gaskill, *Nano Letters* **10**, 39623965 (2010).
- [33] M. M. Parish and P. B. Littlewood, *Nature* **426**, 162 (2003).
- [34] M. M. Parish and P. B. Littlewood, *Physical Review B* **72** (2005).
- [35] A. A. Abrikosov, *Physical Review B* **60**, 4231 (1999).
- [36] A. A. Abrikosov, *Europhysics Letters* **49**, 789 (2000).
- [37] G. Bergmann, *Solid State Communications* **42**, 815 (1982).
- [38] G. Bergmann, *Physics Reports-Review Section of Physics Letters* **107**, 1 (1984).